

Narrow spectral range infrared thermography in the vicinity of 3 μm operating wavelength

by Boris G. Vainer

*Institute of Semiconductor Physics, Russian Academy of Sciences, Siberian Branch,
13, Lavrentyev avenue, Novosibirsk, 630090, Russia, E-mail: vainer@sun20.isp.nsc.ru*

Abstract:

An implementation of infrared thermography (IRT) developed for operation in the narrow spectral range (NSR) close to wavelength λ of 3 μm is presented in detail. Its applicability to remote sensing, multichannel spectrography, optical defectoscopy, medicine, etc. is substantiated. IRT technique for the investigation of low-energy EM sources is described. Basic physical principles, which define room IRT in cosmetology, are specified. A set of advantages of 3- μm -NSR IRT is formulated. System performance of suitable thermographs based on the InAs CID FPA is considered; the linkage between radiation temperature, NETD and frame rate is ascertained. IR camera calibration routine is described.

1. Introduction

Multilateral problems entrusted today to infrared thermography make great demands on the IR cameras. Due to a lack of possibility to create universal multi-purpose thermograph optimal for all radiation temperatures, background levels, target velocities, etc., there is a need to study and develop IRT-method within each of its inner sections.

The most developed regions in IRT are associated with atmospheric-windows (3.5-5.5 μm and (7.5-12) μm . IR detectors based on InSb, PtSi, HgCdTe, GaAs/ $\text{Al}_x\text{Ga}_{1-x}\text{As}$ are usually used in these cases. As a rule, operating spectral diapason of each of those detectors is relatively wide and comprises some micrometers. In the present work, a promising direction in the IRT is circumstantially considered. The main differences from the above are a shorter operating wavelength (2.5-3 μm) and registration of thermal radiation in a narrow band (some tenth parts of micrometer).

2. Thermal radiation in the vicinity of $\lambda = 3 \mu\text{m}$, and an appropriate device for 3- μm -wavelength narrow spectral range IR thermography

Favorable to IRT features of (2.5-3) μm section of the infrared are both a relatively low intensity of terrestrial background radiation and a higher contrast [1]. Narrow enough band near $\lambda=3 \mu\text{m}$ is preferable because shorter waves augment a role of the reflected rays generated by high-temperature natural and/or some artificial light sources. As a result, simple estimations show that NSR IR thermographs with operating wavelengths λ of about 3 μm are quite optimal for work under room conditions (10-30 $^\circ\text{C}$) with objects of about human temperatures (15-45 $^\circ\text{C}$).

There is a number of different ways to realize 3- μm -NSR IRT detecting units. The advanced one is a hybrid microcircuit [InAs focal plane array (FPA)] \leftrightarrow [Si multiplexer] with charge-injected-device (CID)-arranged MIS structures serving as photosensitive cells (similar to presented in [2]). In these detectors, short-wave edge (about 2.5-2.8 μm) is dependent on the degenerated InAs substrate doping level, whereas a long-wave one (near 3.1 μm) is limited by an absorption edge of the operating lowly doped InAs epilayer.

A specific feature of the IRT in question is that the extended section of atmospheric absorption band falls into a working diapason of the detector. The latter is demonstrated in Fig.1 where the atmospheric transmittance spectrum is combined with a particular case of experimentally obtained spectral sensitivity of the InAs-based FPA (128x128) detector used in the present work.

3. Operational factors and performance capabilities of the thermographs

3.1. Detector calibration

Providing high homogeneity in temperature-signal (T-S) transformation over the whole operating 2D-area is an essential problem of the FPA technology. The solution depends to a great extent on an appropriate algorithm for a calibration process, which then allows to perform fast operations with a large data arrays (of the order of 10^4 signals per frame).

As to InAs CID MIS cells, quadratic trinomial is appeared to be a good approximation of measured T-S dependencies. It is demonstrated in Fig.2, where parabolas fit experimental data using the least-squares method. Moreover, it is determined that parabola adequately describes physical behavior of non-saturated CID MIS cell at least at terrestrial temperatures. It justifies the extrapolation of T-S-characteristics outwards from the nameplate temperature range of IRT camera. During calibration, FPA is illuminated from a uniform radiation source with a variable temperature, and the three parabolic coefficients A_i , B_i , and C_i are determined for each i-th photosensitive cell. These coefficients are stored and used when the thermograph is functioning. Temperature T_i corresponding to pixel i is easily determined at any time from the equation $S_i = A_i T_i^2 + B_i T_i + C_i$ (S_i is the current photo-response of i-th cell). Zero drift is compensated by the periodical (1 time per 10 .. 100 min) automatic placing of the built-in reference IR source in front of the FPA.

3.2. Operating speed

Since the procedure of solving the above-mentioned equation needs to be carried out more than 10^4 times per a period of thermogram, maximum speed of operation becomes sensible to the computer processing power. Figure 3 shows the measured values of thermogram rate vs. number of frames N accumulated and averaged to produce one thermogram. For each cell, calculations are made once per N frames (one time per thermogram), therefore it is evident that a larger N – less speed dependence on the processor power. At large N values, speed of operation is mainly limited by the accumulation time of CID. It is presented clearly in Fig.3 where experimental data are compared with the appropriate asymptote.

3.3. Temperature sensitivity

For InAs-based CID FPAs, noise equivalent temperature difference (NETD) analysis must take into consideration the following details: 1) Actual boundaries of the sensitivity spectral range (see Fig.1). 2) Decay of flux due to the atmospheric absorption (with consideration of actual spectral characteristic: Fig.1). 3) Additional filling of CID non-equilibrium potential well with the carriers of non-photoelectric nature (by temperature- and/or field-assisted generation, etc.). 4) Possibility of CID cell to be overflowed at high object temperatures.

In Fig.4, NETD vs. blackbody temperature T is presented. Experimental results were obtained by averaging noise-induced mean square deviations of signal over the whole array of cells. The regime with N=1 was set. Plain cast iron disk covered by turpentine soot was used as a radiation source. Calculations were made in terms of the actual optical scheme, consideration of an additional noise of an electronic section, and items 1)-4) listed above.

It is seen that the experimental NETD decreases with T faster than the calculated one. Partial explanation of this discrepancy could be based on the assumption that the used approach, pertaining to Poisson statistics, is not completely adequate to model charge generation processes in CID cells. For thermal and field-induced mechanisms of generation it was pointed in [3]. Slight rise of experimental curve at high temperatures could be related to the disk temperature fluctuations due to air circulation in the laboratory. This noise-like effect has to be taken into account in a practical IR thermography (e.g. in medical applications).

Figure 5 represents the experimental NETD values vs. thermograph operating speed. Within temperature range used, the data are good linear with the frame rate. From the figure,

it follows that the sensitivity of the thermograph is equal to about $3 \cdot 10^{-2}$ °C at the temperatures near 30°C and frame rate near 10 frame/s. The presented family of curves is obtained at $N=2$. According to Fig.3, measurements with $N=1$ give about the same value of the operating speed. On the other hand, NETD is decreasing with increasing N . As a result, in the present system configuration, which is dependent on the processor power, functioning of the camera at $N=1$ is not optimal. In actual case, $N=2$ has to be chosen as an optimal regime.

4. 3- μm -NSR IRT applications

4.1. Multichannel registration of spatially-distributed spectra

Application of line-array detectors in multichannel spectrometry doesn't allow to perform real-time analysis of the spectra which are non-uniform along the entrance slit of monochromator. The use of FPA-type detector lifts this restriction. Figure 6 shows a segment of atmospheric absorption spectrum in the vicinity of a wavelength $\lambda = 2.65 \mu\text{m}$. It is obtained for 20 ms with the help of InAs-based NSR thermograph placed behind the MUM-3 monochromator with removed output slit (spectrum shown covers just a central segment of FPA). In a simple case presented in Fig.6 the spectrum is varying only in intensity along a vertical line. Though, it is evident that IR radiation produced by spatially-non-uniform process and focused onto the entrance slit could give more complicated spectrogram.

Typical for InAs FPA, narrow spectral band still remains sufficiently wide one for use in special tasks of spectrography. The analysis of IR spectra of known compounds shows that at $\lambda < 3 \mu\text{m}$ absorption spectra of many materials contain strongly pronounced twists, which allow to identify the substance and/or determine its concentration in a mixture. As a proof of it, the only one atlas [4] represents more than 350 organic compounds with strongly marked features within (2.70-3.03) μm band. In this connection, fast 3- μm -NSR IRT cameras could find an adequate use in systems of safety and control in the chemical industry.

4.2. Remote sensing

In spite of the atmospheric absorption effects, it is not an obstacle to use 3- μm NSR IRT for solving some of remote sensing problems. In Fig.7, two corresponding thermograms are shown. They were made at night from an open window located at 15 m above earth level. Thermally inhomogeneous bonnet profile, hot disks, and heads of people inside passenger compartment are well recognized in moving automobile. Thermogram of the 200-m-distant buildings in the figure was obtained at the atmospheric temperature of about +5°C, when snow was still remaining partly on roofs and on earth. Regular structure of light spots belongs to the building windows (the rest four bright spots are images of the street lamps). It should be noted that in the process of measurement, the light inside all rooms was switched off, and the origin of visible spots is the room-temperature radiation emitted from those windows.

4.3. Optical defectoscopy

InAs-based NSR IRT is an optimal tool for a non-destructive control of the concealed unbonded areas at the interfaces of various multi-layer structures [5] (Fig.8). It should be particularly emphasized that operating wavelength $\lambda \approx 3 \mu\text{m}$ allows to reveal quantity, dimensions, and inner relief of defects in both wide-gap (Si, GaAs, GaP, etc.) and relatively narrow-gap ($E_g \geq 0.41$ eV) semiconductors, such as Ge ($E_g = 0.74$ eV), GaSb ($E_g = 0.81$ eV), some compositions of InGaAs, InAsP; the list also includes many of $A^{II}B^{VI}$ semiconductors, etc.

From the FPA NETD investigation, it follows that the cross-sectional noise equivalent error of the method is of the order of 0.01 μm . It allows to display very accurately the profiles of concealed voids and to apply this technique to very thin gaps when interference rings are not formed as yet. In these cases, dimensions and internal structure of defect can be evaluated from a change of image optical density (Fig.9).

4.4. Medicine

According to ch.2, medical thermography is a native area for 3 μ m-NSR IRT. Figure 10 demonstrates three thermograms illustrating different pathological cases. Medical interpretation of those presents no special problems, and the quality of images is not of a secondary importance here.

Although the level of short-wave IR background is relatively low, in medical thermography (as well as in different areas of 3 μ m-NSR IRT applications), proper attention must be given to diffuse and mirror reflection of IR radiation from the objects. It is exhibited in Fig.11. Here, the heated contacts of the overhead daylight lamps were the sources of the reflected rays.

4.5. Cosmetology

Physical and physiological phenomena itemized below prove infrared thermography to be adequately applied to cosmetology:

1. Putting liquid-containing cosmetic means onto human skin is accompanied by an evaporation of the ingredients. It leads treated zones to drop in temperature.
2. Masking (separation from the ambient air) of skin by the cosmetic coatings, as well as the reaction of the coating ingredients with the skin superficial layers, results in the heat-evolution change (under control of the nerve system).
3. Direct injury of skin by a chemical, thermal, radiation or electric burn (from acids, power lasers, etc.), or after some mechanical procedures (peeling, etc.), can lead to either decreasing or increasing skin temperature due to the lymph (or blood) exudation and evaporation, or inflammation, respectively.
4. Thermally active hardware or manual treatments (steaming, etc.) induce heat transmitting into the skin, and cause its proper thermal reaction (heating, or cooling by perspiration).
5. Thermally passive treatments (massage, low-intensity EM radiation exposure, etc.) can induce changes in blood circulation in the superficial vessels. The latter causes associated changes in the heat-evolution intensity.
6. Durable change in thermal image of the skin can be an objective indicator of the efficiency in cosmetic treatments provided.

IRT gives cosmetologist an insight into the processes usually hidden from his eyes. As an example, Fig.12 represents in detail the behavior of skin temperature during one of the thermally active cosmetic treatments (ozone-admixed steaming). A noticeable downward excursion of temperature in forty seconds after commencement of procedure enables one to trap the moment of abrupt increase in activity of sweat glands. With the help of 3 μ m-NSR IRT we also showed that time dependence of skin temperature after moistening or sponging by spirit is logarithmic. A typical time required to return the skin to initial temperature is about 7-8 min when moistening and about 1-2 min when sponging by spirit.

In beauty salon, IR camera offers a prospect of real-time control over the quality of performing various cosmetic treatments. Two associated examples are demonstrated in Fig.13. Additional argumentation for the usefulness IRT in cosmetology can be found in [6].

4.6. Investigation of the temperature profiles of warm streams and sprays

Ozone-admixed steaming represented in Fig.13 was carried out with a stream of a hot steam. To IR thermograph, it looks like a "hot flame", and its spatial profile can be revealed and displayed. A sustaining example is presented in Fig.14. It is observable how initially fine-bored flow transforms into the broad zone as it meets an obstacle (a client's face).

4.7. Visualization of the radiation directional diagram of low-energy EM sources

To investigate output characteristics of complex irradiators combining a group of low-energy EM sources, both high-sensitive and multi-diapason detectors are needed. Recently

essayed technique [7] allows leaving out these complicative requirements. The scheme of this method is presented in Fig.15. Radiation flow is incident on the surface of a thin black-body-like screen. Low heat capacity of the screen leads to fast heating. On the other hand, low tangential thermal conductivity makes thermal pattern impossible for becoming blurred. Finally, IR camera located behind (as it is shown), or in front of the screen, registers the originated thermal picture. Described converter makes it possible to study EM sources of almost all spectral bands with the help of the only one thermograph.

An example of the associated thermogram is presented in Fig.16. Here, the radiation directional diagram not far from a sharp optical head of the magnetic-infrared-laser therapeutic apparatus is shown. Four IR diodes, which generate EM radiation near $0.9\ \mu\text{m}$, are responsible for the four elongated “petals”, whereas the semiconductor pulsed $0.89\text{-}\mu\text{m}$ -laser produces a bright spot in the central part of the thermogram.

5. Conclusion

A direction in infrared thermography, which is characterized by the operating wavelengths near $3\ \mu\text{m}$ and a narrow spectral range, has unique capabilities to solve a lot of IRT tasks in terrestrial conditions. InAs FPA-based IR thermographs are attractive for use as $3\text{-}\mu\text{m}$ -NSR IRT devices.

Working narrow band near wavelength $3\ \mu\text{m}$ is likely to be as an optimal choice in many respects. This is particularly true in optical defectoscopy when the compromise is required between diversity of valid materials and cross-sectional resolution of the inspection method.

In addition, narrow-banded IR imaging systems allow simplifying the requirements to a lens by optimizing that only to a special (operating) wavelength. The advantages of this technique are less complicated antireflection coatings, negligible chromatic aberration, etc.

Acknowledgements

The author would like to thank V.Ya.Belenky and L.I.Fomina for their kind putting cosmetic salon “Viola” at author’s disposal for carrying out the associated experiments; Dr. I.I.Lee for useful discussions devoted to general points on NETD.

References

- [1] WOOLAWAY, J.T. , “New sensor technology for the 3- to $5\text{-}\mu\text{m}$ imaging band”, *Photonics Spectra*, vol.25, No.2, 1991, p 113-119
- [2] KURYSHEV, G.L., KOVCHAVTZEV, A.P., VAINER, B.G., et al., “Medical infrared imaging system based on a 128×128 focal plane array for $2.8\text{-}3.05\ \mu\text{m}$ spectral range”, *Optoelectronics, Instrumentation and Data Processing (Autometria)*, 4,1998, p 5-10
- [3] KHALIULLIN, N.I. , “Dark- and background-generated charge fluctuations in the CID detectors of radiation”, *Microelectronica*, vol.16, No.5, 1987, p 463-465 (in Rus.)
- [4] SCHRADER, B., “Raman/Infrared atlas of organic compounds”, Second edition, VCH Verlagsgesellschaft mbH, 1989, 1120 pp
- [5] VAINER, B.G., KAMAEV, G.N., and KURYSHEV, G.L., “Application of the narrow spectral range InAs-FPA-based IR camera for the investigation of the interface voids in silicon wafer bonding”, *J.Crist.Growth*, vol. 210, No.1-3, 2000, p 351-355
- [6] BELENKY, V.Ya., and VAINER, B.G. “Thermovision method for controlling cosmetic products effect on human skin”; in: 2nd International Scientific-Practical Conference “Biologically Active Substances and New Cosmetic Product” (abstracts), 24-26 November, 1997, Moscow, PCAR, 1997, p 118
- [7] VAINER, B.G., BELENKY, V.Ya., and KHRISTOFOROV, V.N. “The use of infrared thermography for characterization of low-energy radiation sources”, a lecture given at the 6th International Scientific-Practical Conference on Quantum Therapy, Moscow, 6-10 December, 1999.

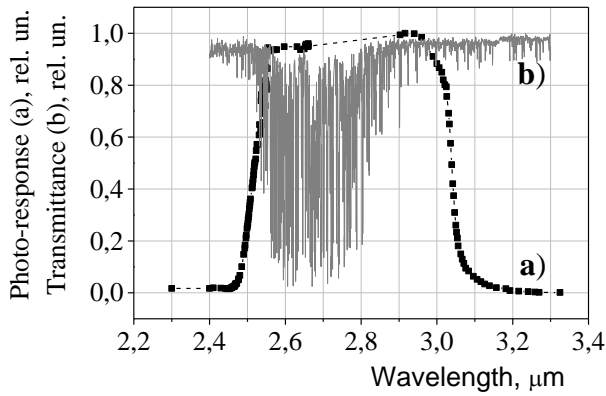


Figure 1: Spectral sensitivity of the InAs FPA-based NSR IR thermograph (a), and atmospheric transmittance (b).

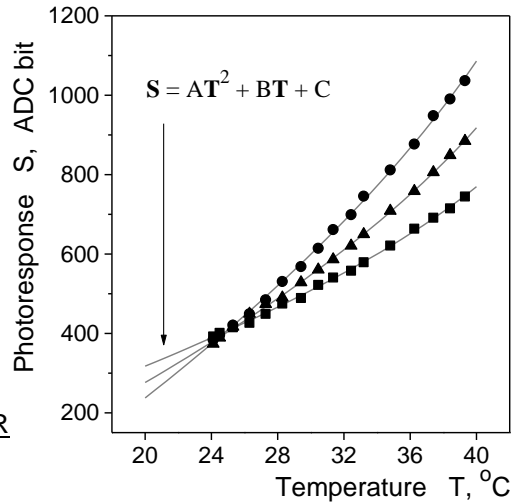


Figure 2: Calibration data obtained from three cells (points), and approximating curves (solid).

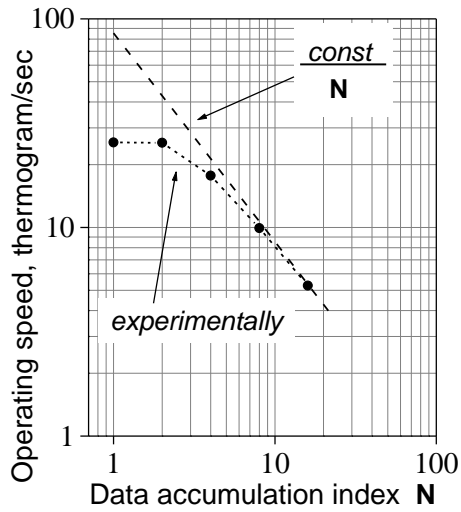


Figure 3: Operating speed of thermograph.

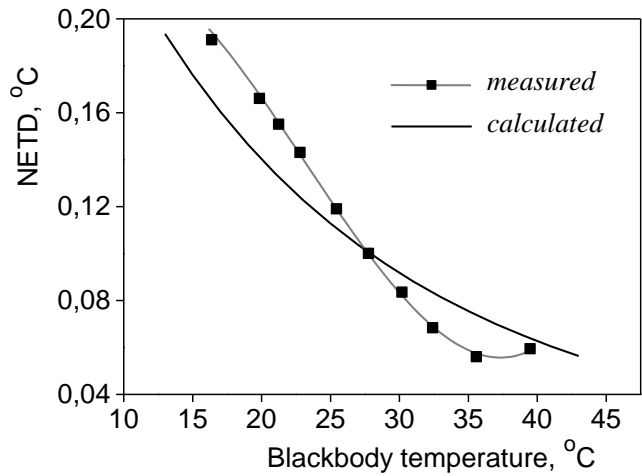


Figure 4: Noise equivalent temperature difference vs. target radiation temperature.

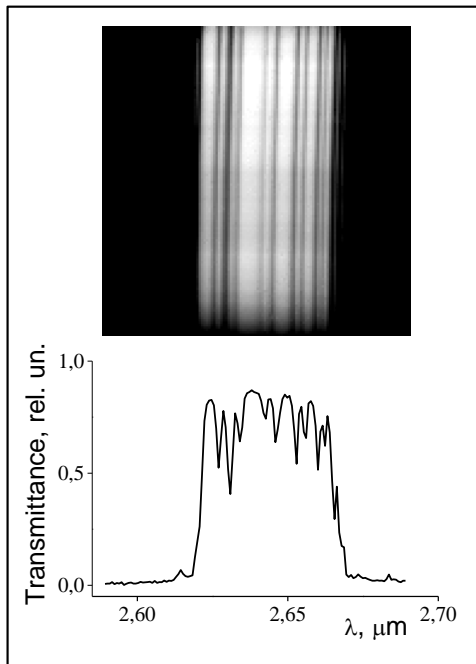


Figure 6: The segment of atmospheric transmittance spectrum measured by NSR IRT camera.

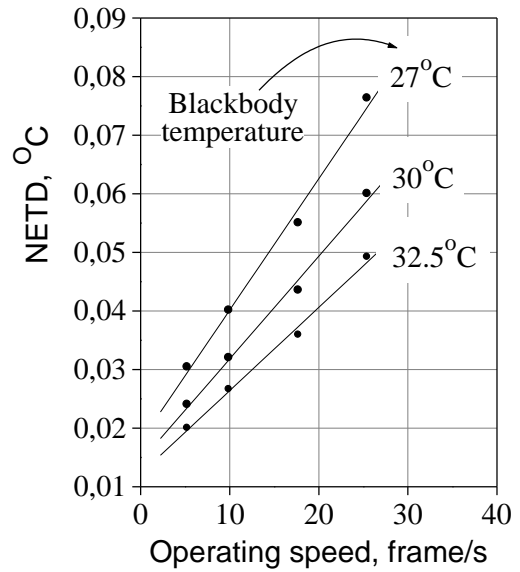


Figure 5: Noise equivalent temperature difference vs. frame rate.



Figure 7: Thermoqrms of the remote objects.

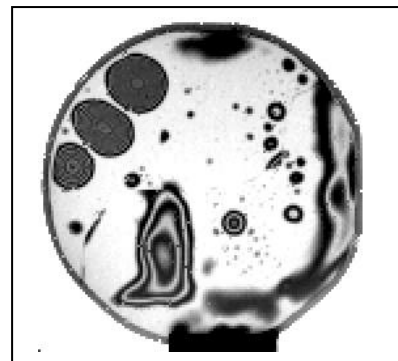


Figure 8: Concealed defects (voids) between two silicon wafers.

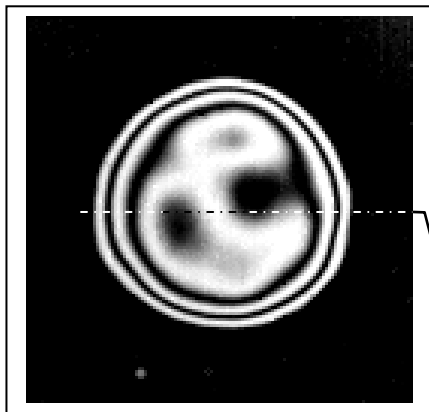


Figure 9: Concealed defect with complicated inner relief, and evaluation of its structure with the 3- μ m-NSR-IRT thermograph.

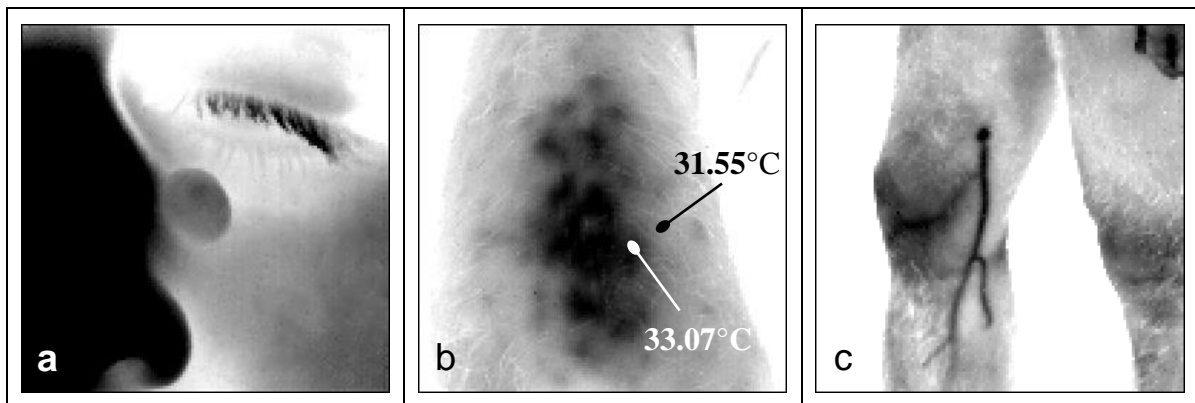
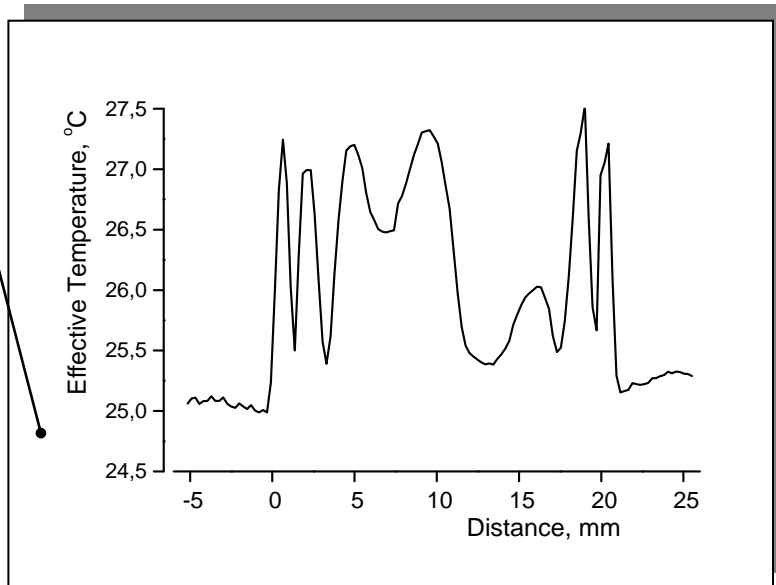


Figure 10: a. Benign tumor close to nose. b. Thermal structure of the posttraumatic inflammation of the left arm (negative). c. Varicophlebitis of the right leg (negative).

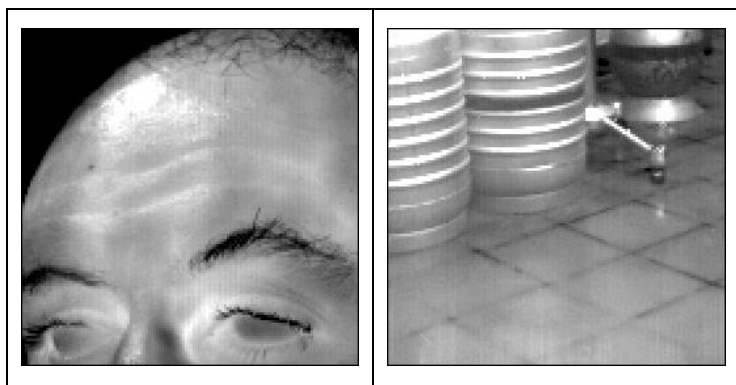


Figure 11: Flash on the forehead (left); IR-reflection image (right).

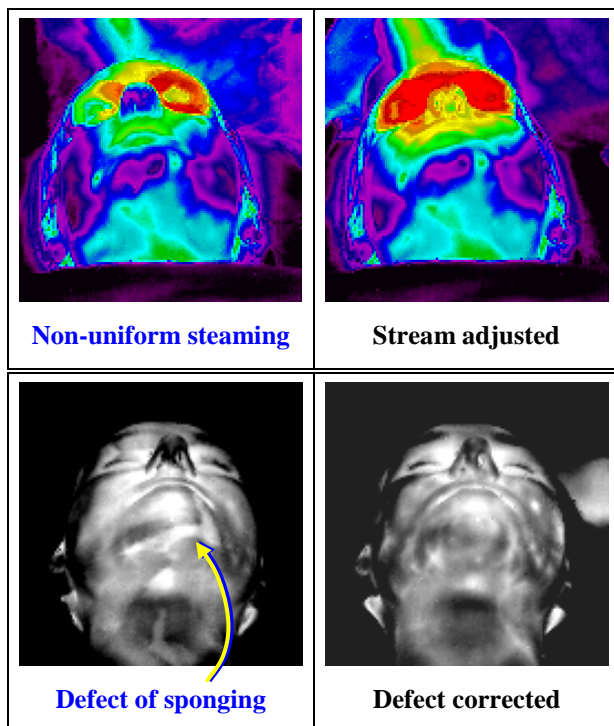


Figure 13: Ozone-admixed steaming (top), and effect of incomplete sponging by tonic (bottom).

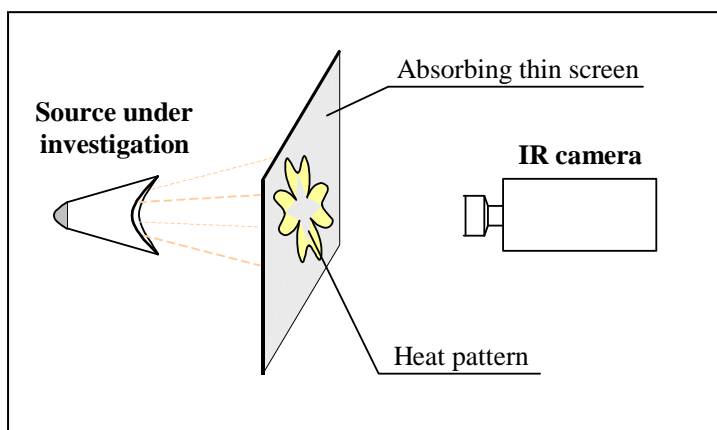


Figure 15: Scheme of the thermographic investigation of low-energy electromagnetic sources.

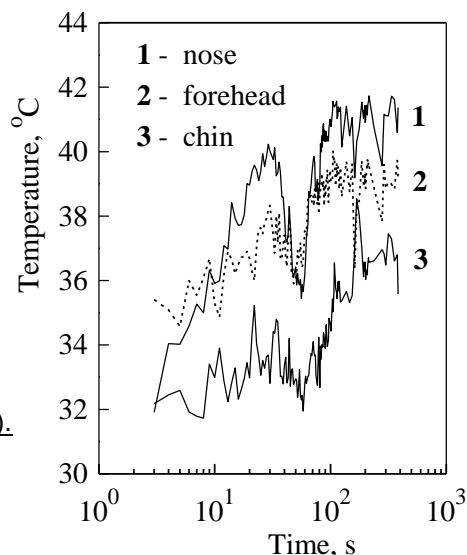


Figure 12: Face temperature instability in process of cosmetic steaming.

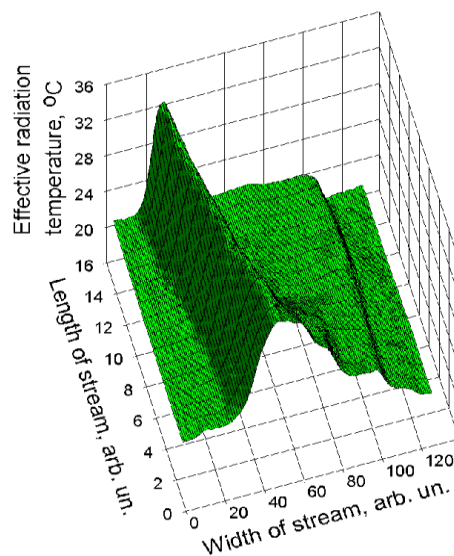


Figure 14: Effective temperature spatial relief of a warm steam stream.

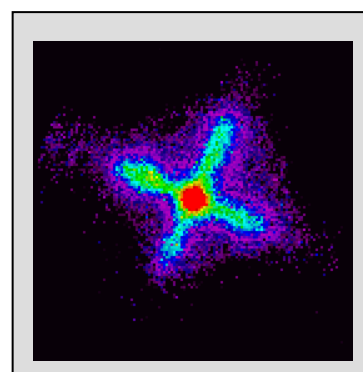


Figure 16: Heat pattern near joint EM source.